Tunable Stability and Performance of Fused Thienothiophene Based Polymers for Organic Electrochemical Transistors and Artificial Synapse Based on A Side Chain Reorganization Strategy

Liao, Hailiang; Luo, Linqu; Wang, Yazhou; Shan, Wentao; Yang, Yu Ying; Luke, Joel; Marsh, Adam V.; Martín, Jaime; Savva, Achilleas; More Authors

DOI
10.1002/adma.202512687

DOI
Dutch Copyright Act (Article 25fa)

Publication date
2025

Document Version
Final published version

Published in
Advanced Materials

Advanced Materials

ADVANCED MATERIALS
www.advmat.de

RESEARCH ARTICLE

Tunable Stability and Performance of Fused Thienothiophene Based Polymers for Organic Electrochemical Transistors and Artificial Synapse Based on A Side Chain Reorganization Strategy

Hailiang Liao[1] | Linqu Luo[1] | Yazhou Wang[2] | Wentao Shan[2] | Yu-Ying Yang[1] | Joel Luke | Adam V. Marsh[1] | Tania Cecilia Hidalgo Castillo[2] | Adel Hama[2] | Hendrik Faber[1] | Xabier Rodríguez-Martínez[3] | Jaime Martín[3] | Achilleas Savva[4] | Thomas D. Anthopoulos[5] | Sahika Inal[2] | Martin Heeney[1]

[1]Division of Physical Science and Engineering, Chemistry Program, King Abdullah University of Science and Technology (KAUST), Thuwal, Saudi Arabia | [2]Organic Bioelectronics Laboratory, Biological and Environmental Science and Engineering Division, King Abdullah University of Science and Technology (KAUST), Thuwal, Saudi Arabia | [3]Centro de Investigación en Tecnoloxías Navais e Industriais (CITENI), Universidade Da Coruña, Campus de Esteiro s/n, Ferrol, Spain | [4]Department of Microelectronics, Faculty of Electrical Engineering, Mathematics and Computer Science, Delft University of Technology, Delft, Netherlands | [5]Henry Royce Institute and Photon Science Institute, Department of Electrical and Electronic Engineering, The University of Manchester, Manchester, UK

Correspondence: Martin Heeney (martin.heeney@kaust.edu.sa)

Received: 3 July 2025 | **Revised:** 10 December 2025 | **Accepted:** 10 December 2025

Keywords: artifical synapse | extreme temperature stability | mixed ionic electronic conductors | organic electrochemical transistors | side chain reorganization

ABSTRACT

We report a series of novel polymeric mixed ionic-electronic conductors based upon the incorporation of fused thieno[3,2-*b*]thiophene and bithiophene with isomeric sidechains. The enhanced rigidity in the polymer backbone facilitated the formation of stabilized bipolarons, while the reorganized ethylene glycol side chains not only maintained the polymer's hydrophilicity but also unexpectedly enhanced the crystallinity of the polymer film. This design strategy led to the development of 4gTT-2gT, a high-performance and stable organic mixed ionic-electronic conductor. The polymer exhibited a maximum μC^* of 729 F V^{-1} cm^{-1} s^{-1}, one of the highest values among low-threshold voltage polythiophene derivatives, while demonstrating excellent operational stability, retaining 99% of its maximum current after 1-h device switching cycles and 94% after 9-h at lower bias. We implemented the material in OECT-based artificial synapses, which maintained functionality under a large temperature range (23–373 K). These combined properties establish 4gTT-2gT as a prime candidate for next-generation mixed conductor devices.

1 | Introduction

Organic electrochemical transistors (OECTs) have garnered significant attention as transformative devices that operate via the bulk doping and dedoping of organic mixed ionic-electronic conductors (OMIECs) upon interaction with ions from an electrolyte [1–4]. Their compatibility with aqueous electrolytes enables this bulk (de)doping process and, in turn, gives OECTs several features that are desirable for next-generation bioelectronic and neuromorphic systems, including high transconductance at low operating voltages, compatibility with aqueous environments, and mechanical softness [3, 5–8]. Over the past decade, OECTs have evolved from simple sensing components into multifunctional platforms capable of signal amplification, logic operations, memory storage, and dynamic information processing [9–13]. Recent breakthroughs in OMIECs have further expanded their

utility, enabling devices such as implantable neural probes, sweat-based metabolite sensors, and adaptive artificial synapses that mimic biological learning [11, 14, 15]. As the functionality and complexity of OECT-based systems expand, the development of high-performance OMIEC materials becomes increasingly critical. However, exploiting the full potential of OECTs requires striking a balance between charge carrier mobility and volumetric capacitance, conventionally expressed as the figure of merit μC^*, together with other practically important metrics such as switching speed, operating voltage, and long-term operational stability under complex physiological conditions [1, 16, 17]. This challenge underscores the need for innovative polymeric systems that balance ionic permeability, electronic conductivity, and structural robustness [1, 18].

Side-chain engineering has emerged as a powerful strategy for tuning the performance of OMIEC materials [19]. Increasing the length of hydrophilic poly(ethylene glycol) (PEG) side chains has been shown to enhance ion accessibility and doping efficiency by improving polymer hydrophilicity [20, 21]. However, excessively long PEG chains can disrupt the crystallinity of the conjugated backbone, compromising mixed ionic-electronic conduction and leading to irreversible electrochemical degradation due to excessive water uptake [17, 22, 23]. To balance ionic transport and structural integrity, the introduction of hydrophobic segments into the side chains has become a widely adopted design strategy [19, 24]. For instance, transforming fully PEG side chains into hybrid alkyl-ether side chains improves film stability by reducing water absorption [24], while further tuning the alkyl spacer length enables systematic modulation of polymer–electrolyte interactions [25, 26]. Additionally, incorporating hydrophobic alkylated moieties along the backbone can suppress electrochemical degradation by limiting water penetration [27–29]. However, such hydrophobic modifications often sacrifice electronic performance to gain stability [30]. Recently, side chain reorganization, in which the distribution of side chain lengths along the backbone is varied, leading to a reduction of symmetry, has emerged as a promising alternative, offering a route to enhance long-term device stability without sacrificing (and in some cases even improving) electronic performance and altering overall side chain length [31]. Despite its potential, this strategy remains underexplored in OMIEC polymer design.

In addition to side-chain engineering, the design of the conjugated polymer backbone plays a pivotal role in OECT performance [1]. Among the high-performance polymer materials reported to date, a wide variety of donor-acceptor (D-A) type polymers have dominated the field, with some achieving exceptional μC^* values as high as 847 F V^{-1} cm^{-1} s^{-1} [22]. However, many D-A polymers exhibit high threshold voltages, which significantly limit their operational window and can result in devices with high energy consumption, as well as increasing the likelihood of undesired side reactions [32–36]. In contrast, all-donor polymers such as polythiophene derivatives bearing PEG side chains exhibit a desirable combination of high performance and low threshold voltages, making them promising candidates for OECT channel materials [20, 31, 37, 38]. However, their device performance is limited by moderate charge carrier mobility (μ). One approach to improve charge transport, extensively investigated in the development of materials for organic field-effect transistors (OFETs), is the replacement of backbone thiophene with a fused thieno[3,2-*b*]thiophene (TT) [39]. The fused nature of TT can increase backbone planarity and rigidity, which enhances π-conjugation and facilitates stronger intermolecular π–π stacking, leading to improved charge carrier mobility [40].

Some of the first polymers developed for OECTs incorporated unsubstituted TT units with PEGylated bithiophene (2gT) comonomers [37]. Later work examined the use of a diPEGylated TT (gTT) monomer in all-donor or D-A type co-polymers [32, 41–43]. Despite their promising performance, we note that for OFET type polymers, dialkylTT groups were found to reduce charge carrier mobility [39]. This was speculated to relate to the coupling of both side chains to the same TT monomer, such that any ring movement requires the cooperative motion of both alkyl chains, which could hinder the formation of the optimal coplanar conformation on solidification from solution. As such, we consider that mono PEGylated TTs, which to the best of our knowledge have not been previously reported, were attractive targets for inclusion into all-donor polymer derivatives.

Here we report a new class of polymers incorporating extended π-conjugation by introducing a novel bithieno[3,2-*b*]thiophene (2TT) backbone. Both TT units featured a single PEG side chain and were coupled in a head-to-head fashion, and co-polymerized with a PEGylated bithiophene (2gT). Simultaneously, we test the hypothesis that reorganizing the distribution of PEG sidechains along the backbone can be used as a rational design strategy to optimize ionic-electronic transport balance and operational stability. Through systematic molecular design and screening, we identified 4gTT-2gT as the most promising candidate, achieving a maximum μC^* of 729 F V^{-1} cm^{-1} s^{-1}, one of the highest among polythiophene derivatives, along with a low threshold voltage of −0.04 V, fast response times of 342 µs (τ_{on}) and 122 µs (τ_{off}), and excellent operational stability under cyclic pulsing over extended duration, with the device channel current still retaining 94% of its initial value after 9 h of operation. Beyond its transistor performance, we further demonstrate its applicability in electrochemical random access memory (ECRAM) devices for synaptic plasticity. The resulting devices exhibit excellent artificial synaptic functions and operate reliably across a wide temperature range (233–373 K), highlighting their robustness and versatility. These results not only establish an important step forward for organic mixed ionic-electronic conductors (OMIECs), but also open new avenues for advanced OECT-based devices in harsh and dynamic environments.

2 | Results and Discussion

The synthesis route to the mono PEGlyated TT monomer, and is subsequent coupling in a head-to-head fashion is shown in Figure 1a. Briefly, trimeric (3 g), tetrameric (4 g), and pentameric (5 g) side chains were introduced by the reaction of 3-methoxythieno[3,2-*b*]thiophene with the respective methoxy capped ethylene glycol oligomer under acid catalyzed conditions. Subsequent mono-bromination occurred in the more activated 2-position, and the resulting bromide was dimerized in a head-to-head fashion by treatment with one-half equivalent of hexabutyldistannane in the presence of a palladium catalyst. The resulting dimer (TT) was brominated with NBS and co-polymerized with 5,5'-bis(trimethylstannyl)-2,2'-bithiophene (T)

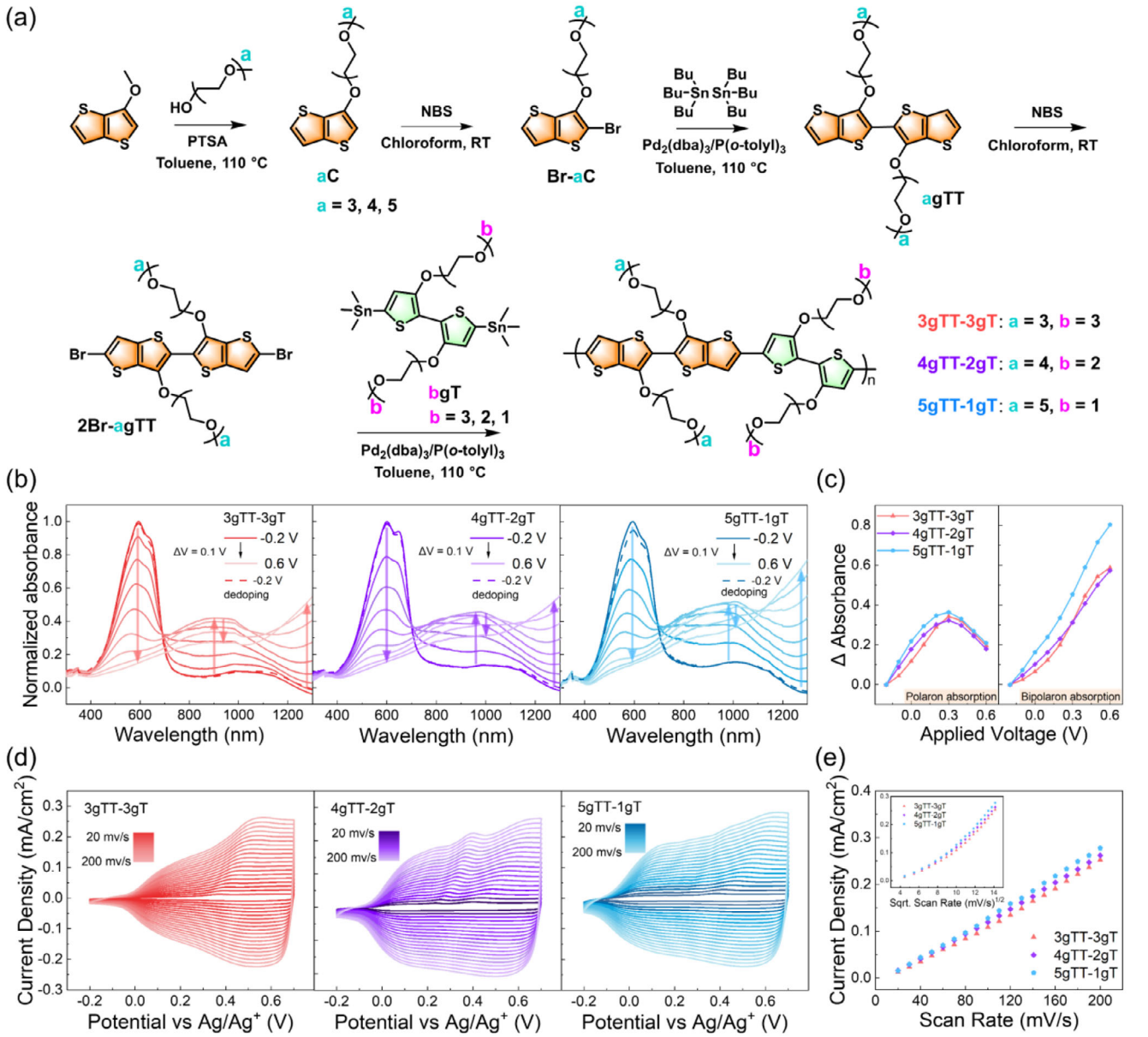

FIGURE 1 | (a) Synthesis route of target polymers. (b) Potential-dependent UV–vis–NIR polymer film absorption spectra of 3gTT-3gT, 4gTT-2gT, and 5gTT-1gT. (c) Absolute changes in polaron (900 nm) and bipolaron (1300 nm) absorption of films vs. applied bias. (d) 20–200 mV s^{-1} scan rate dependence CV of 3gTT-3gT, 4gTT-2gT, and 5gTT-1gT in 0.1 M aqueous NaCl solution. (e) Peak currents vs. scan rates, with the inset displaying peak currents against the square roots of scan rates.

comonomers bearing complementary glycol side chains under Stille polymerization conditions. The total number of ethylene glycol oligomers across the two monomers was kept as six, distributed either evenly in 3gTT-3gT, or asymmetrically in 4gTT-2gT, and 5gTT-1gT.

All polymers were purified by soxhlet washing followed by extraction with chloroform. They exhibited good solubility in chloroform, enabling facile solution processing at room temperature. The pronounced aggregation of the polymers at room temperature prevented the acquisition of ^{1}H NMR spectra under ambient conditions. As a result, high-temperature ^{1}H NMR measurements were conducted to confirm the polymer structures. The series of polymers all exhibited a well-resolved spectrum at 393 K, with all environments clearly resolved (Figures S25–S27).

Their molecular weights were determined using analytical gel permeation chromatography (GPC) with hexafluoroisopropanol as the solvent (Table 1). Although there was some variance across the series, they were all in the high weight regime and exhibited good film-forming properties. Attempts to increase the molecular weight of 4gTT-2gT and 5gTT-1gT to similar values of 3gTT-3gT by varying the polymerization time or concentration were not successful. The series of polymers exhibited no significant weight loss below 150°C, demonstrating good thermal stability within this temperature range, as determined by thermogravimetric analysis (TGA) (Figure S28). All three polymers showed an initial weight-loss step around 150°C, which corresponded well with the glass transition temperature (Tg) peaks observed in the DSC measurements. This initial mass loss is likely due to the release of a small amount of trapped water, attributed to the inherent

TABLE 1 | Optical and electronic properties.

Polymers	$\lambda_{max,\ film}$ (nm)	$\lambda_{onset,\ film}$ (nm)	$E_{g,opt}$ (eV)[a]	E_{HOMO} (eV)[b]	E_{LUMO} (eV)[c]	M_n (kDa)/$Đ$[d]
3gTT-3gT	596	1240	1.00	−4.58	−3.58	169.8/4.22
4gTT-2gT	623	1235	1.00	−4.46	−3.46	95.2/2.37
5gTT-1gT	602	1206	1.03	−4.48	−3.45	107.3/1.67

[a]Derived from the absorption onset of polymer film ($E_{g,opt} = 1240/\lambda_{onset,film}$).
[b]E_{HOMO} was estimated by photoelectron spectroscopy in air. Error is ± 0.05 eV.
[c]E_{LUMO} was calculated by the equation $E_{LUMO} = E_{HOMO} + E_{g,opt}$.
[d]GPC calculated number average molecular weight (M_n) and dispersity ($Đ$) by GPC against polystyrene standards.

hydrophilicity of the polymers. A second, more substantial weight-loss step was observed at approximately 280°C, suggesting the onset of polymer degradation, likely by side chain breakdown.

The normalized ultraviolet–visible-near infrared (UV–vis–NIR) absorption spectra of polymer thin films are depicted in Figure S29a, and the detailed optical properties are summarized in Table 1. Solution spectra are shown in Figure S30. The polymer films exhibit broadly similar absorption spectra, with maximum absorption peaks around 600 nm. For 3gTT-3gT, λ_{max} occurs at 596 nm, with a relatively clear vibronic shoulder observed at longer wavelengths (631 nm). For 5gTT-1gT the shoulder is less well resolved, and the maxima occurs at 602 nm. For 4gTT-2gT the shoulder is the most intense peak, resulting in a maxima absorption of 623 nm. Given that absorption spectra are sensitive to short range packing effects and π–π overlap, the spectra highlight that side chain reorganization can clearly influence packing. This likely facilitated the formation of a more ordered stacking structure, promoting stronger intermolecular π–π coupling, resulting in the red-shifted absorption [44]. Differences in the solution UV/Vis absorption as a function of temperature are also noted (Figure S30), in which 3gTT-3gT shows more disaggregation on heating, suggestive of less pronounced aggregation in solution.

Notably, all spectra display a distinct broadened low-energy shoulder (~700–1200 nm), which is much more pronounced for 4gTT-2gT and 5gTT-1gT compared to 3gTT-3gT. Combined with spectroelectrochemical results (Figure 1c), this phenomenon may be associated with environmental doping effects. Under non-inert conditions (air exposure), oxygen and water molecules act as electron acceptors to p-dope the conjugated backbones, generating polaronic or bipolaronic states and thus introducing additional low-energy shoulder peaks in the absorption spectra [45, 46]. When a reverse bias of –0.2 V was applied to de-dope the polymer films, the intensity of the polaron absorption peaks of all three polymers was reduced to similarly low levels, indicating that the doped states can be reversibly suppressed through electrochemical control. However, at 0 V, the polaron absorption intensity of 3gTT-3gT was significantly lower than that of 4gTT-2gT and 5gTT-1gT, indicating that the latter two are more prone to spontaneous doping upon exposure to air.

The ionization potential of the polymer films was measured via photoelectron spectroscopy in air (PESA), and these values were used to estimate the highest occupied molecular orbital (HOMO) energy levels. The lowest unoccupied molecular orbital (LUMO) energies were calculated by adding the optical bandgap (derived from the onset point of film absorption spectra) to the HOMO values. All energy levels are summarized in Table 1. It is noteworthy that the HOMO energy levels of 4gTT-2gT and 5gTT-1gT are remarkably close, positioned at –4.46 and –4.48 eV, respectively. These values exhibit a significant upward shift of $\Delta E \approx 0.10$ eV compared to 3gTT-3gT (–4.58 eV). The elevated HOMO levels enhance the energy level alignment between the conjugated backbone and oxygen molecules (acting as electron acceptors), thereby increasing the susceptibility of 4gTT-2gT and 5gTT-1gT to oxidation. This thermodynamic preference further rationalizes the appearance of polaron absorption shoulder peaks in their spectra (Figure S29a), which arise from the stabilized charge-transfer states induced by ambient doping [45].

Spectroelectrochemical measurements were performed in 0.1 M NaCl aqueous electrolyte to investigate the polymers' doping mechanism. The electrochromic responses when the applied bias moved from −0.2 to 0.6 V under ambient conditions for 3gTT-3gT, 4gTT-2gT, and 5gTT-1gT are shown in Figure 1b. As a comparison, Figure 1c and Figure S29b show the absolute changes in absorption peaks for all three polymers, where this is clearly discernible. Across the series, their spectra exhibit a consistent trend under applied bias, the intensity of the π-π^* absorption band decreases gradually due to the electrochromic effect, accompanied by the appearance of a new band around 900 nm, assigned to polaron formation. At higher bias, the intensity of the polaron band starts to decrease, and a longer wavelength peak (with a maxima > 1300 nm) grows in, indicative of bipolaron formation [47, 48]. We note that bipolaron formation has recently been shown to enhance film stability and charge transport properties through strengthened interchain electronic coupling and reduced defect-mediated recombination [27]. It can be observed that polaron absorption peaks begin to emerge when a voltage of –0.1 V is applied, indicating that the series of polymers can undergo ion doping even under slightly negative bias. As the applied bias voltage gradually increases, the π-π^* transition peak intensities of all three polymers exhibit continuous attenuation, while the polaron absorption peak intensities follow a non-monotonic trend that initially increases, reaching saturation at 0.3 V, and subsequently decaying due to the conversion of polarons to bipolarons. Concurrently, the bipolaron absorption peak intensity steadily rises with increasing voltage. Notably, although 3gTT-3gT and 4gTT-2gT exhibit comparable bipolaron polarization degrees, 5gTT-1gT displays significantly higher bipolaron generation efficiency. This discrepancy likely correlates with differences in film crystallinity, as revealed by GIWAXS (grazing-incidence wide-angle X-ray scattering) analysis, vide infra, with 5gTT-1gT adopting a relatively disordered molecular packing structure. Bipolarons have been found to preferentially

TABLE 2 | Summary of the characteristics of OECTs.

Polymer	d [nm]	V_{Th} (V)[a]	$g_{m,norm}$ (S cm^{-1})[b]	μC^* (F V^{-1} cm^{-1} s^{-1})[c]	μC^* (F V^{-1} cm^{-1} s^{-1})[d]	C^* (F cm^{-3})[e]	μ (cm^2 V^{-1} s^{-1})[f]	τ_{on} (μs)	τ_{off} (μs)	$\tau_{i,on}$ (μs)	I_{on}/I_{off}
3gTT-3gT	61.3 ± 1.1	−0.18	296 ± 3	505 (499 ± 6)	504	158 ± 14	3.20 ± 0.28	1020	212	421	10^3
4gTT-2gT	43.0 ± 1.5	−0.04	395 ± 13	729 (705 ± 24)	717	171 ± 6	4.26 ± 0.15	342	122	240	10^3
5gTT-1gT	41.5 ± 0.5	−0.05	174 ± 2	331 (327 ± 4)	310	171 ± 10	1.94 ± 0.11	340	126	182	10^3

[a]Values determined by extrapolating the corresponding $I_D^{1/2}$–V_G plots.
[b]The average transconductance values normalized by the channel geometry.
[c]Maximum and average data calculated from the equation: $g_m = WdL^{-1}\mu C^*(V_{Th} - V_G)$.
[d]Extracted from the fitting of g_m vs. $(WdL^{-1})(V_{Th} - V_G)$ plots (Figure S33).
[e]Data deduced from the slop of different effective volumetric capacitance.
[f]Data obtained from the μC^* and the volumetric capacitance C^*.

form in disordered regions [49]. However, reduced crystallinity may compromise the operational stability and carrier transport capacity in organic electrochemical transistors (OECTs) [17].

We collected scan rate dependent cyclic voltammograms (CV) data from −0.2 to 0.7 V in 0.1 M NaCl aqueous electrolyte (Figure 1d), revealing that all polymers exhibit surface-controlled electrochemical behavior. As shown in Figure 1e, the peak currents of the redox processes for the three polymers display a linear relationship with the scan rate, deviating from the diffusion-controlled mode predicted by the Randles–Sevcik equation (where peak currents scale with the square root of the scan rate). This characteristic indicates that the charge storage mechanism is dominated by surface-controlled Faradaic processes, where the current originates from rapid redox-state switching of the polymer film and synergistic electric double-layer charging/discharging, rather than being limited by ion diffusion kinetics, and suggests that all polymers possess good charge transport properties [50]. Consequently, even at high scan rates (e.g., 1000 mV/s), no current attenuation due to mass transport hysteresis was observed (Figure S31). Combined with their flexible processability, these materials demonstrate significant application potential in flexible supercapacitors and wearable electronics.

OECT devices were fabricated to evaluate the mixed ionic and electronic transport characteristics of these novel polymers. The output and transfer characteristics of the OECTs are shown in Figure 2, and the corresponding data is summarized in Table 2. All polymers behaved as p-type accumulation mode OECTs. The initially designed polymer in this series was 3gTT-3gT, which exhibited a threshold voltage of –0.18 V, a normalized transconductance ($g_{m,norm}$) of 296 ± 3 S cm^{-1}, and a corresponding maximum μC^* of 505 F V^{-1} cm^{-1} s^{-1}. Upon side chain reorganization of the molecular backbone, the resulting polymer 4gTT-2gT showed a significant reduction in threshold voltage to –0.04 V, along with a substantial increase in channel current. Its $g_{m,norm}$ improved to 395 ± 13 S cm^{-1}, while the maximum μC^* reached 729 F V^{-1} cm^{-1} s^{-1}, placing it among the top-tier p-type OECT polymers reported to date [36]. Further reorganization of the side chains yielded 5gTT-1gT, which maintained the same threshold voltage (–0.05 V) but exhibited a reduced $g_{m,norm}$ of 174 ± 2 S cm^{-1} and a lower μC^* of 331 F V^{-1} cm^{-1} s^{-1}. Without altering the conjugated backbone or the total glycol chain content, we successfully optimized the polymer structure through the side chain reorganization process, yielding 4gTT-2gT as the best-performing material in this series.

Interestingly, among the series of polymers, 3gTT-3gT exhibited the highest molecular weight. To exclude the possibility that the observed performance differences originate solely from variations in molecular weight, and since we were not able to increase the molecular of 4gTT-2-gT, we instead fractionated 3gTT-3gT using preparative GPC to obtain samples with different Mn values. As shown in Figure S34, when the molecular weight of 3gTT-3gT decreased, the OECT performance of the polymer also decreased, with the fraction exhibiting the molecular weight analogous to that of 4gTT-2gT exhibiting the worse device performance. This suggests that the differences observed arise mainly from the variation in sidechain distribution, rather than molecular weight. It also highlights that further improvements in the performance of 4gTT-2gT might be expected if the molecular weight could be improved, for example by catalyst optimization.

Notably, most high μC^* p-type polymers reported to date suffer from excessively high threshold voltages (see further discussion in Figure S35). This limitation results in narrow operational voltage windows and significantly increased device power consumption. Moreover, high driving voltages can induce undesirable electrochemical side reactions or polymer degradation, severely constraining their potential applications in bioelectronics [51]. In contrast, 4gTT-2gT exhibits a low threshold voltage of −0.04 V, potentially enabling high sensitivity in detecting weak bioelectrical signals [52, 53]. The low threshold voltage originates from the polymer's redox onset occurring near 0 V, indicative of its rapid ion-electron coupling kinetics. Consequently, 4gTT-2gT enables efficient and energy-saving operation under ultralow working voltages, mitigating risks of electrochemical side reactions and preventing electrical stimulation damage to biological tissues.

The decay time constants for the ON (τ_{on}) and OFF (τ_{off}) processes of these polymers were extracted by fitting the temporal response curve with the exponential decay equation $I_D(t) = I_{D,0} + A \times \exp(-t/\tau)$ (Figure S36) [33], and are summarized in Table 2. The τ_{on} / τ_{off} values were evaluated to be 1020/212, 342/122, and 340/126 μs for 3gTT-3gT, 4gTT-2gT, and 5gTT-1gT, respectively. The series of polymers exhibit rapid response speeds that are higher than those of the most advanced materials currently available [32–36]. We performed frequency-domain gate current analysis to estimate the impedance matched response time ($\tau_{i,on}$) of the

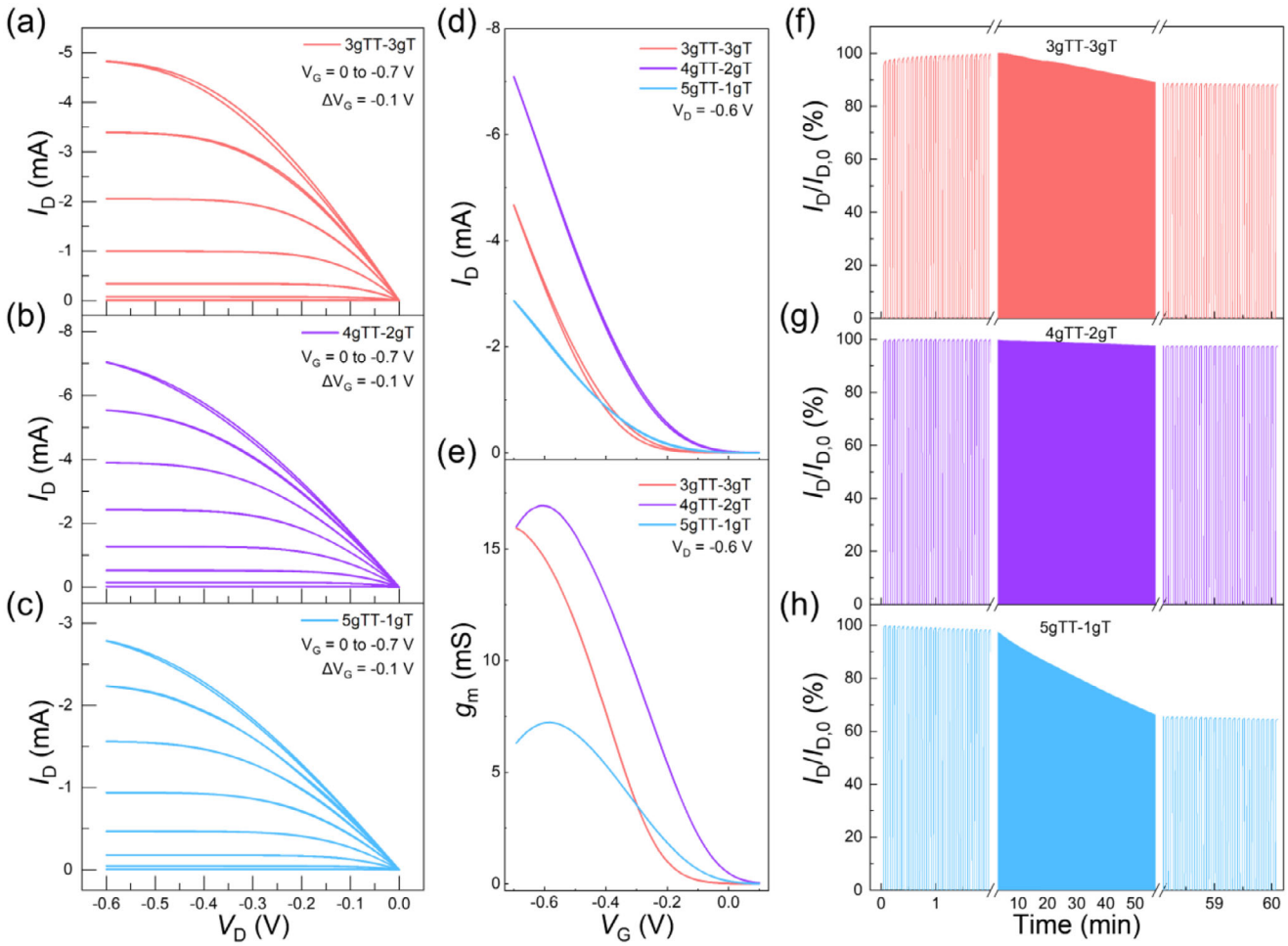

FIGURE 2 | OECTs output curves of (a) 3gTT-3gT, (b) 4gTT-2gT, and (c) 5gTT-1gT at stepped V_G from 0 to −0.6 V in 0.1 V intervals. (d) Transfer and (e) corresponding transconductance curves of the various polymers at $V_D = -0.6$ V. Operational stabilities of (f) 3gTT-3gT, (g) 4gTT-2gT, (h) 5gTT-1gT, with 60 min of 720 on-off electrochemical cycles ($V_D = -0.5$ V; $V_G = 0$ to −0.5 V).

series of polymers in OECTs (Figure S37) and compared them with the channel response times. The results are summarized in Table 2, showing that $\tau_{i,on}$ of the three polymers are 421, 240, 182 µs, respectively, which are consistent with the corresponding channel response times. To facilitate comparison with the literature, we show μC^* values as the primary figure of merit. Given recent discussion surrounding mobility estimation, we also evaluated the mobility via an impedance matched method (see Supplementary Information), which demonstrates an identical mobility trend, albeit with lower values [54, 55].

The long-term operational stabilities of polymers were also investigated by monitoring the variation of drain current upon applying successive pulse bias (pulse length = 2.5 s) (Figure 2f–h). Experimental results revealed that the maximum current of 3gTT-3gT decayed to 88% of its initial value after 1 h of operation, while 5gTT-1gT exhibited even poorer operational stability, retaining only 65% of its initial current, likely due to its inferior film crystallinity. In contrast, 4gTT-2gT not only demonstrated the best OECT performance metrics but also maintained good stability, retaining 99% of its initial current after continuous operation for 1 h, dropping to 92% after 2 h and 1440 switching cycles (Figure S38). Additionally, we also probed stability at a lower bias voltage (Figure S39) [56]. After 9 h of operation, the device channel current still retained 94% of its initial value. We also note that OECT operational stability is not solely dependent on the active semiconductor, but is also strongly influenced by factors such as electrode monolayers, device geometry, electrolyte composition, and biasing conditions, and optimization of these parameters may lead to further improvements [4, 55, 57]. This observation strongly validates side-chain reorganization as a beneficial design strategy in enhancing material stability. Notably, 4gTT-2gT uniquely combines high μC^* value (729 F V^{-1} cm^{-1} s^{-1}), a low threshold voltage (−0.04 V), and good operational stability, distinguishing it from all reported polythiophene-based OECT polymers (as discussed in Figure S32). This attractive combination underscores its potential for flexible electronics applications, particularly in next-generation wearable biosensors, low-power neuromorphic devices, and biocompatible interfaces requiring both high performance and long-term reliability.

Electrochemical impedance spectroscopy (EIS) measurements were performed to evaluate the volumetric capacitances (C^*) of all polymers (Figure S40). As shown in Figure 3a, the C^* of 3gTT-3gT, 4gTT-2gT, and 5gTT-1gT were 158 ± 14, 171 ± 6, 171 ± 10 F cm^{-3}, respectively. The volumetric capacitance of the polymer series exhibited some variation, but remained within a relatively narrow range. The water contact angles of the series were measured to

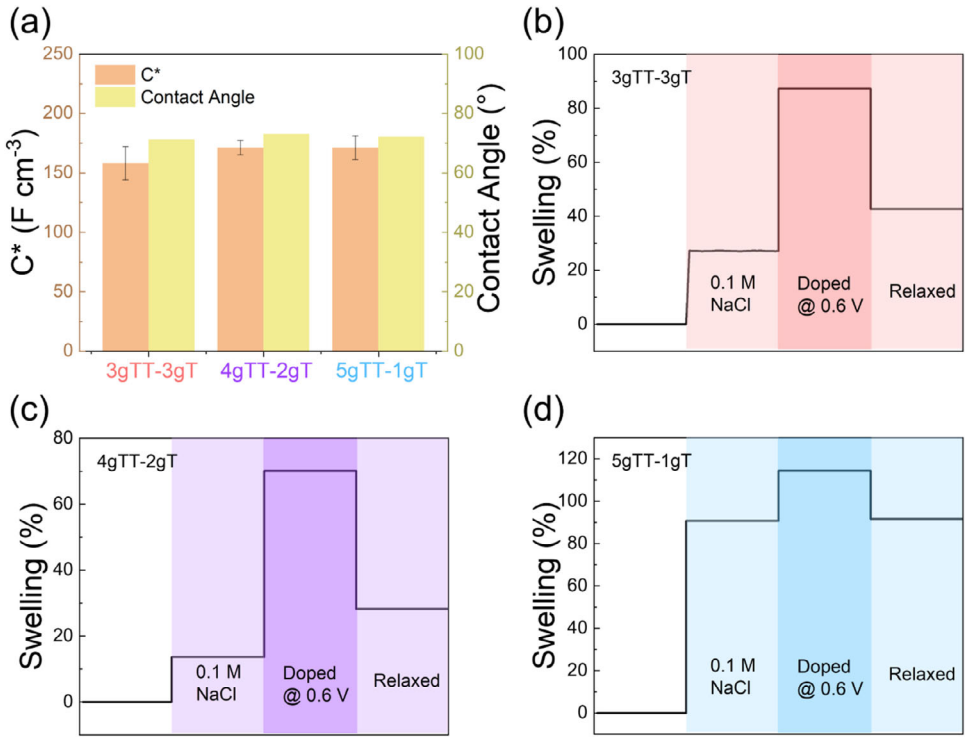

FIGURE 3 | (a) Volumetric capacitances (left, orange) and contact angle (right, yellow) of a series of polymers. (b) The film thickness swelling changes of 3gTT-3gT, (c) 4gTT-2gT, and (d) 5gTT-1gT as monitored by electrochemical quartz crystal microbalance with dissipation monitoring (EQCM-D) after sequential exposure to 0.1 M NaCl solution, electrochemical doping, and relaxation.

be 71.3°, 73.1°, and 72.1°, respectively (Figure S41). This minor difference is likely due to the unchanged total alkoxy content in the side chains during the reorganization process, resulting in similar surface hydrophilicity among the three polymer films.

To investigate the electrochemical stability of the polymer series during ion doping, we employed an electrochemical quartz crystal microbalance with dissipation monitoring (EQCM-D) to study the interaction between the polymer films and the electrolyte solution during both passive swelling and voltage-driven active swelling (Figure 3b–d, and square wave voltage are shown in Figure S43). During the initial passive swelling stage in 0.1 M NaCl electrolyte, the swelling ratios of 3gTT-3gT, 4gTT-2gT, and 5gTT-1gT were 27%, 14%, and 90%, respectively. Although the percentage of glycol side chains is the same for each polymer, their relative distribution clearly strongly influences water uptake, which corresponds well with device stability. 5gTT-1gT displayed the most pronounced water uptake, which is strongly correlated with its lower film crystallinity, as revealed by GIWAXS analysis, vide infra. Upon application of a 0.6 V bias to trigger active swelling, the swelling ratios increased to 87%, 70%, and 114%, respectively, indicating enhanced swelling driven by the synergistic insertion of ions and water under the electric field. After removing the bias, 4gTT-2gT demonstrated superior recovery, with its swelling ratio falling back to 28%, followed by 3gTT-3gT (40%), whereas 5gTT-1gT only recovered to 91%. These distinct swelling behaviors are closely related to the material's electrochemical stability. The drastic volumetric fluctuations of 5gTT-1gT (90% → 114% → 91%) under bias can induce interfacial stress accumulation during ion doping/de-doping, potentially leading to morphological disruption and electrochemical degradation. In contrast, the reduced volume change of 4gTT-2gT (14% → 70% → 28%) effectively mitigates mechanical fatigue caused by repetitive charge/discharge cycles, thereby maintaining long-term device stability [51]. This highlights the critical role of low swelling behavior in ensuring the mechanical reliability of flexible electronic devices.

To investigate the morphological evolution of the polymer films during electrochemical doping/dedoping processes, we characterized the surface morphologies of the three polymers in their pristine, doped, and dedoped states using atomic force microscopy (AFM) (Figure 4a). For 3gTT-3gT, the pristine film exhibited a roughness of 1.85 nm with some localized porous structures apparent. Upon electrochemical doping, the roughness decreased to 1.08 nm, accompanied by pore closure and surface flattening. After dedoping, the roughness further reduced to 0.97 nm, but the surface morphology remained similar to the doped state without restoring the initial porous features, indicating irreversible structural reorganization. In contrast, 4gTT-2gT demonstrated improved morphological stability, with the pristine film showing a roughness of 1.67 nm with fibrous microcrystalline structures apparent. Doping slightly reduced the roughness to 1.49 nm, while the fibrous striations became sharper and more defined due to ion intercalation. Remarkably, dedoping restored the roughness to 1.58 nm, with the fibrous morphology transitioning back to the pristine homogeneous state, confirming structural integrity of the crystalline domains throughout the doping cycle. 5gTT-1gT, behaved significantly differently. Its pristine film displayed a high roughness of 2.98 nm with abundant pores visible. Doping abruptly reduced the roughness to 0.83 nm and closed the pores, whilst dedoping did not restore the morphology of the film

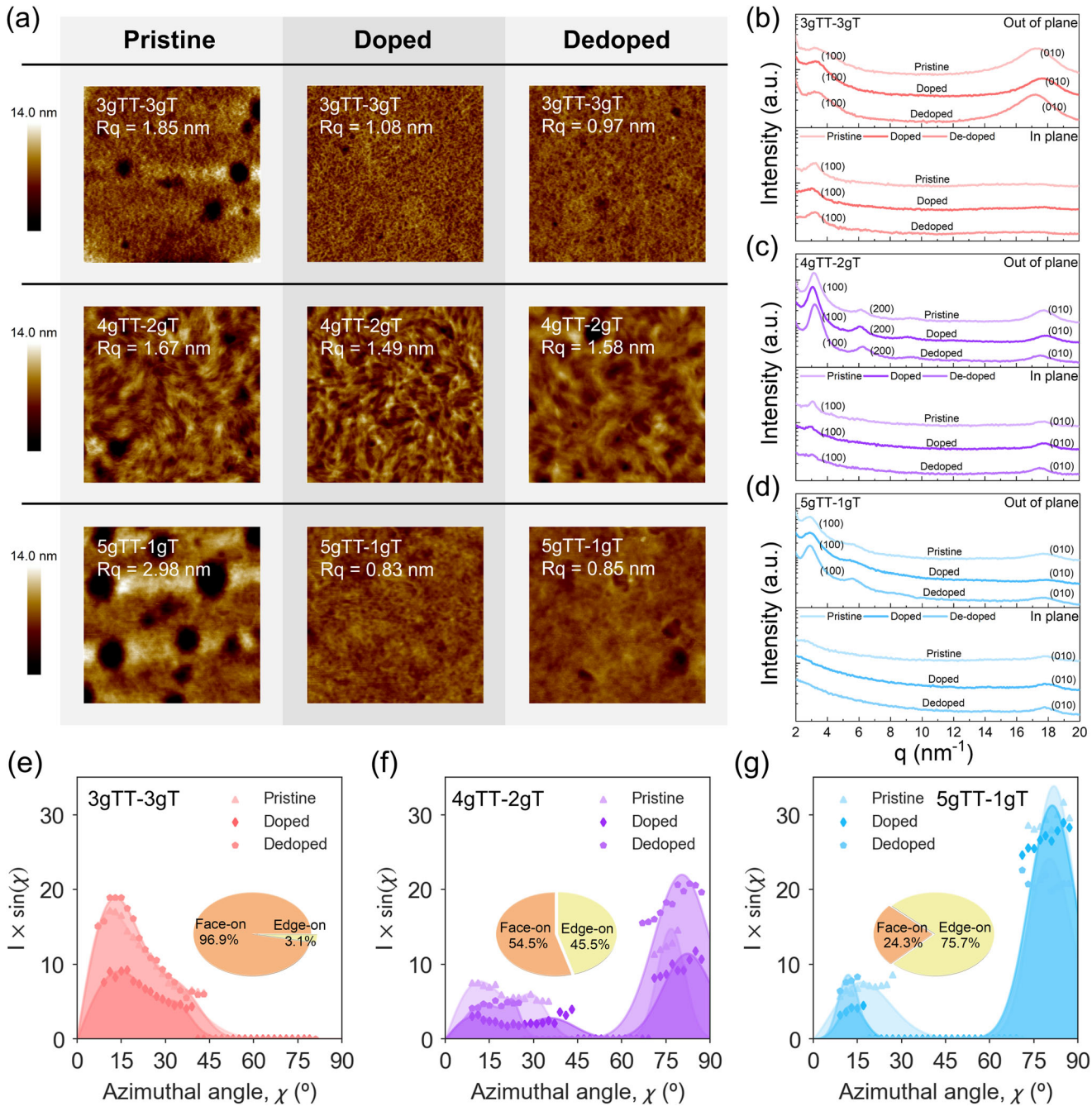

FIGURE 4 | (a) Atomic force microscopy (AFM) images of 3gTT-3gT, 4gTT-2gT, and 5gTT-1gT films in three states: pristine, doped at 0.6 V for 5 min, de-doped at −0.2 V for 5 min, the image size is 1 × 1 micron. Grazing incidence wide-angle X-ray scattering (GIWAXS) line-cut profiles of the (b) 3gTT-3gT, (c) 4gTT-2gT, and (d) 5gTT-1gT films in the in-plane and out-of-plane directions. The pole figure of the integration along the azimuthal angle of the (010) peak of (e) 3gTT-3gT, (f) 4gTT-2gT, and (g) 5gTT-1gT in pristine, doped, and de-doped states, with the corresponding pristine state face-on/edge-on population insert.

to its initial state, with roughness remaining at 0.85 nm, revealing irreversible structural changes during ion insertion/extraction. The morphological differences highlight how side chain reorganization can influence film morphology, with the microcrystalline fibrous network of 4gTT-2gT apparently helping with mechanical robustness during the doping/dedoping process.

To further investigate the structural evolution of the polymer films during electrochemical doping/dedoping, we also conducted grazing incidence wide-angle X-ray scattering (GIWAXS) analyses on the series of polymers in their pristine, doped, and dedoped states (Figure 4b–d; Figure S44 and Table S1). For 3gTT-3gT, the line cuts of pristine film exhibited a weak out-of-plane (100) peak at q_z = 3.25 nm^{-1} (lamellar d-spacing: 1.93 nm) and a broad (010) peak at q_z = 17.24 nm^{-1} (π–π stacking distance: 0.36 nm), together with an in-plane (100) peak indicative of face-on-dominated packing. Upon doping, the (100) peak slightly shifted to 3.29 nm^{-1} (1.90 nm d-spacing) while the (010) peak slightly moved to 17.70 nm^{-1} (0.35 nm stacking). After dedoping, both out-of-plane (100) and (010) peaks nearly reverted to their

original positions. Meanwhile, the in-plane (100) peak shifted reversibly from q_{xy} = 3.25 nm^{-1} (pristine, 1.93 nm d-spacing) to 3.10 nm^{-1} (doped, 2.02 nm d-spacing) and back, suggesting reversible lamellar adjustments.

For 4gTT-2gT, its pristine film showed a sharp out-of-plane (100) peak at q_z = 3.14 nm^{-1} (lamellar spacing 2.00 nm) together with a distinct second order (200) peak at q_z = 6.15 nm^{-1}, suggesting more highly ordered lamellar stacking enabled by the side-chain reorganization. Doping slightly shifted the (100) peak to 3.05 nm^{-1} (2.06 nm d-spacing), while the (010) peak remained unchanged (17.24 nm^{-1}, 0.36 nm stacking). And dedoping restored the (100) peak to the original position, while the (010) peak remained unchanged at q_z = 17.24 nm^{-1}. The in-plane direction also showed reversible (100) peak shifts (pristine: q_{xy} = 3.13 nm^{-1} → doped: 3.03 nm^{-1} → dedoped: 3.11 nm^{-1}) and stable (010) peak. The persistence of (010) peaks in both out-of-plane and in-plane directions suggests its electrochemical stability of 4gTT-2gT during the doping and dedoping process. For 5gTT-1gT, its pristine film showed an out-of-plane (100) peak at q_z = 2.89 nm^{-1} (2.17 nm d-spacing) and a (010) peak at q_z = 17.77 nm^{-1} (0.35 nm stacking). Doping caused the (010) peak to vanish, and dedoping only weakly restored it, with the in-plane (010) peak (17.81 nm^{-1}) unchanged during the doping and dedoping process.

To further analyze the crystallinity evolution of the series of polymer films during the doping and dedoping processes, we obtained pole figures along the azimuthal angle of the (010) reflection (Figure 4e–g) and extracted the integrated (010) peak area (Table S2), which serves as an effective quantifiable indicator of film crystallinity. Based on the (010) integrated intensity distribution in the ranges $0° < \chi < 45°$ (face-on) and $45° < \chi < 90°$ (edge-on), the corresponding face-on/edge-on ratios were determined (as shown in Figure 4e–g insert). 3gTT-3gT primarily shows face-on oriented packing, with an initial (010) integrated area of 8.26. Upon doping, the crystallinity decreased by 48%, while dedoping led to an effective recovery (+4%). 4gTT-2gT exhibits a mixed face-on/edge-on stacking configuration, which could facilitate a hybrid transport mechanism in mixed ionic-electronic conductors by providing efficient ion penetration channels through the face-on orientation (vertical direction) while maintaining charge transport stability via the edge-on orientation (horizontal direction). Among the series of polymers, 4gTT-2gT exhibits the lowest initial crystallinity. Upon doping, its crystallinity decreased by 20%. However, after dedoping, the crystallinity not only recovered but was further enhanced (+44%). 5gTT-1gT adopts a predominantly edge-on stacking configuration with the highest initial crystallinity. After doping, its crystallinity decreased by 16%, and rather than recovering during dedoping, it was further reduced (–30%). The crystallinity evolution of the three polymers during the doping/dedoping process is consistent with the results observed from EQCM-D and AFM measurements.

Overall, side-chain reorganization was found to have clear structural and morphological consequences. GIWAXS revealed that 4gTT-2gT maintained reversible lamellar order and stable π–π stacking during doping/dedoping (unchanged (010) peaks in both out-of-plane and in-plane directions), with an overall crystallinity enhancement after dedoping. By contrast, 3gTT-3gT and 5gTT-1gT showed less stable ordering and irreversible changes in their surface morphology. EQCM-D confirmed that 4gTT-2gT underwent markedly less swelling than either 3gTT-3gT or 5gTT-1gT, while AFM showed that its fibrous morphology recovered after dedoping, unlike the incomplete recovery observed for the other polymers. These results indicate that reorganization of side chains reduces swelling, stabilises crystalline domains, and improves morphological robustness, which together explain the enhanced stability and mixed conduction of 4gTT-2gT compared with its analogues.

To further evaluate the potential of 4gTT-2gT for future electronic applications, we investigated its performance in artificial synaptic devices. Bio-inspired neuromorphic devices enable energy-efficient adaptive learning through synaptic plasticity emulation, advancing brain-like computing and intelligent systems evolution [58]. Artificial synaptic systems emulate biological neurons' action potential driven information processing. Electrical pulses applied to the gate electrode, which mimics a pre-synaptic neuron, are used to modulate the injection and extraction of ions between the ionic gel and the semiconducting channel [59, 60]. The resulting change in channel conductance, which is analogous to the post-synaptic current, is measured as the current flowing between the source and drain electrodes [61]. Notably, solid-state ion-gel electrolytes enable non-volatile conductance states in OMIECs through their confined ion diffusion dynamics, making them suitable for OECT-based electrochemical random-access memories (ECRAMs) devices [59, 62, 63]. Therefore, to investigate the synaptic behavior of 4gTT-2gT-based devices, we fabricated ECRAMs using a solid-state ion-gel composed of polymeric insulator poly(vinylidene fluoride-co-hexafluoropropylene) (PVDF-HFP) and ionic liquids 1-butyl-3-methylimidazolium bis(trifluoromethylsulfonyl)imide (BMIM:TFSI) as electrolyte, and characterized them under ambient conditions.

For spike-amplitude-dependent plasticity (SADP), the excitatory postsynaptic current (EPSC) was recorded upon spiking the presynaptic voltages ($V_{G,\,pre}$) pulses (100 μs in width) from −0.1 to −0.7 V in a stepwise (0.2 V steps) manner. As shown in Figure 5a, the peak value of the EPSC exhibits a linear relationship with the applied pulse voltage. Due to limitations in the device's ion diffusion kinetics, the EPSC does not immediately return to its initial state during the interval between voltage pulses, but instead decays gradually [62–64]. By regulating the single pulses duration (t_{pre}) from 20 μs to 1000 μs, spike-timing-dependent plasticity (STDP) synaptic behavior was simulated (Figure 5b). The EPSC peak gradually increases with the increase in pulse duration, after the applied voltage is removed, the EPSC gradually decreases. For spike-number-dependent plasticity (SNDP), a series of $V_{G,\,pre}$ pulses (−0.5 V with a width of 40 μs) ranging from 10 to 200 were applied to the gate electrode, while a constant bias of −0.5 V was maintained between the source and drain (Figure 5c). The corresponding pulse-number-dependent EPSC peak and memory level were extracted, as shown in the inset of Figure 5c. As the number of pulses increases, the EPSC gradually rises and eventually saturates. Following the removal of the pulsed input, devices stimulated with a higher number of pulses exhibit enhanced memory levels, defined as the EPSC measured after a 5 ms retention period at 0 V. These series of tests demonstrate the potential of 4gTT-2gT-based ECRAMs for bio-inspired applications.

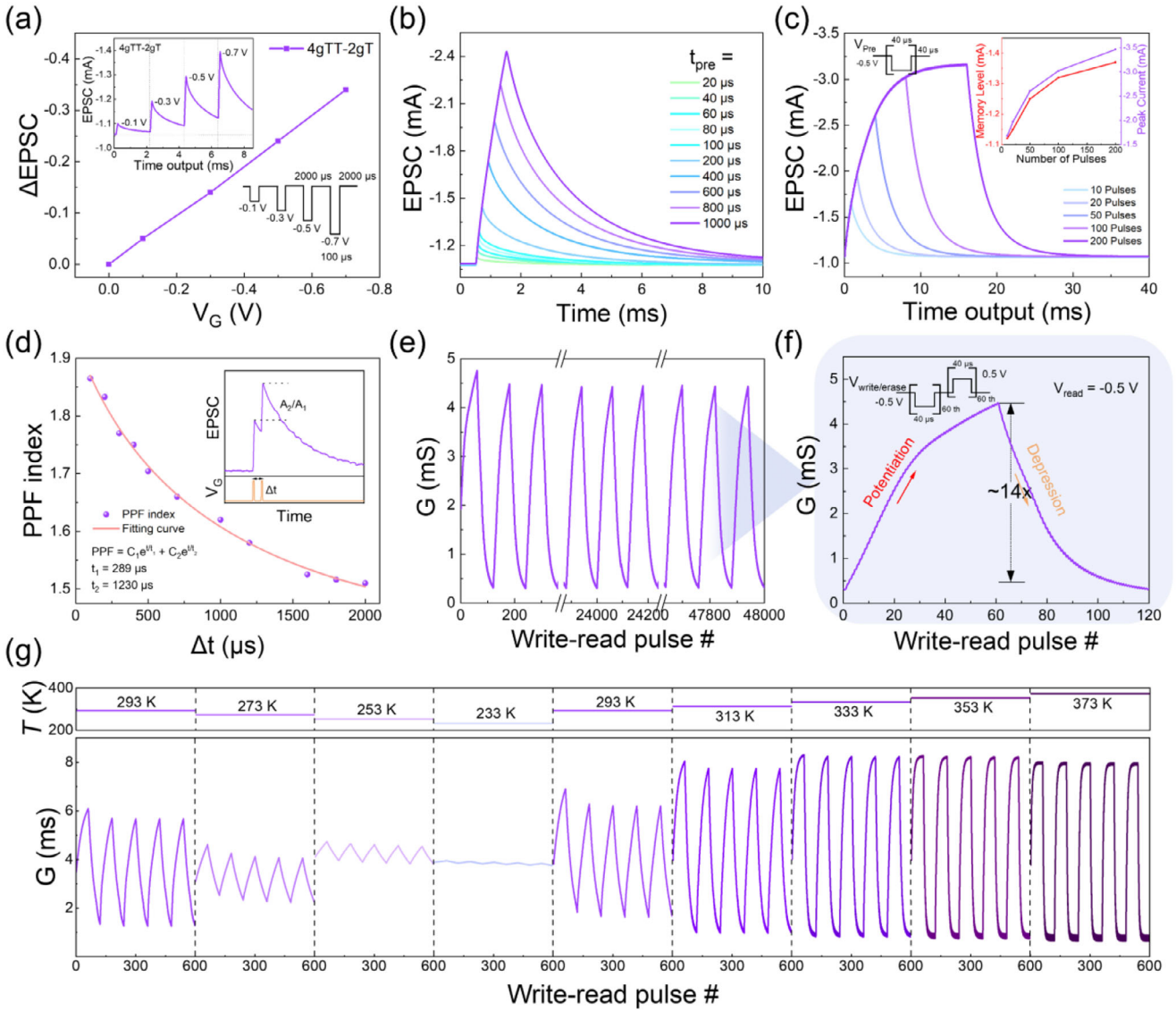

FIGURE 5 | The characteristics of OECT-based electrochemical random-access memories (ECRAMs) with solid-state ionic gel. (a) Spike-amplitude-dependent plasticity (SADP) of 4gTT-2gT device with different $V_{G,\,pre}$ ranging from −0.1 to −0.7 V, under V_D = −0.5 V, t_{pre} = 100 μs, Δt_{pre} = 2000 μs. (b) spiking-timing-dependent plasticity (STDP) of 4gTT-2gT device with different spike time ranging from 20 μs to 1000 μs, under $V_{G,\,pre}$ = −0.5 V, V_D = −0.5 V. (c) Spike-number-dependent plasticity (SNDP) of 4gTT-2gT, triggered by different spike numbers. (Inset shows the memory level as the excitatory post-synaptic current (EPSC) after holding the channel for 5 ms at 0 V and peak current with varying pulse numbers, on Y1 and Y2 axis, respectively). (d) PPF index of 4gTT-2gT device. The purple circle and red line are the experimental PPF index and fitted result, respectively. The inset is a schematic of how such biasing is typically realized. (e) Cyclic long-term depression and potentiation (LTDP) behavior of 4gTT-2gT under voltage control. 60 repeated potentiation pulses (V_{write} = −0.5 V, t_{pre} = 40 μs, Δt_{pre} = 40 μs) and 60 repeated depression pulses (V_{erase} = 0.5 V, t_{pre} = 40 μs, Δt_{pre} = 40 μs) indicate a cycle. (f) One representative LTDP cycle. (g) Five LTDP cycles were performed at each temperature during the stepped transitions of 4gTT-2gT device, varying from 293 K down to 233 K, back to 293 K, and then up to 373 K. The temperature change tests were conducted under high-vacuum conditions.

Furthermore, two successive pulses (−0.5 V, t_{pre} = 40 μs) with varying pulse intervals (Δt_{pre}) ranging from 100 μs to 2000 μs were applied to investigate paired-pulse facilitation (PPF), a key indicator of synaptic tunability. As quantified in Figure 5d, the PPF index was defined as A_2/A_1, where A_1 and A_2 represent EPSC amplitudes from first and second pulses, respectively [60]. Experimental data followed a biexponential decay: $PPF = A_1\exp(-\Delta t/\tau_1) + A_2\exp(-\Delta t/\tau_2)$ (τ_1 = 289 μs, τ_2 = 1230 μs, R^2 = 0.996). During Δt_{pre}, dynamic ion redistribution occurred through counterion migration from electrolyte to channel, forming transient electron-ion complexes that modulated EPSC decay kinetics, a process governed by the interpulse interval. 4gTT-2gT-based ECRAMs showed a maximum facilitation value of 186% at Δt_{pre} = 100 μs with gradual decay to 150% at 2000 μs, demonstrating precise temporal control.

Building on the demonstrated potential of 4gTT-2gT-based ECRAMs for efficient electrochemical modulation and retention, we further evaluated their synaptic endurance through repeated cycles of long-term potentiation and depression (LTDP). As shown in Figure 5e,f, the LTDP (long-term depression and potentiation) characteristics of the device exhibit highly linear and

symmetric conductance modulation across consecutive cycles of potentiation and depression pulses. One full cycle consists of 60 write and 60 erase pulses, and even after 400 cycles (equivalent to 48 000 write/read pluses), the channel conductance range remains stable without degradation. The device also demonstrates excellent operational endurance under ambient conditions, featuring a microsecond-level write/read speed and an ultrawide conductance dynamic range of over 14×, comparable to state-of-the-art materials [59]. These attributes fully satisfy the high-precision and high-dynamic-range requirements of neuromorphic computing systems.

Leveraging the LTDP characteristics of the 4gTT-2gT-based artificial synapse, we implemented backpropagation training within a three-layer neural network using the CrossSim simulator for image recognition tasks by extracting the measured switching conductance states (100 cycles). The neural network was simulated on the MNIST dataset (28 × 28 pixels), and achieved a recognition accuracy of approximately 88% after 30 training epochs (Figure S45b). Furthermore, the corresponding confusion matrix illustrates accurate classification across all ten handwritten digits (Figure S45c), highlighting the promise of 4gTT-2gT for analogue neuromorphic computing applications.

Operational endurance and thermal stability are critical prerequisites for the integration of organic ECRAMs into conventional electronics intended for real-world deployment [59]. Therefore, to investigate the tolerance of the ECRAMs under complex thermal environments, conductance (G) cycling tests were performed under vacuum with a stepped temperature gradient, conducting five cycles at each temperature. As shown in Figure 5g, the initial measurement was taken at 293 K. As the temperature decreased stepwise, the dynamic range of G modulation gradually narrowed. However, pronounced conductance modulation was still clearly observed, even down to 233 K. Notably, upon returning to 293 K, the conductance range fully recovered to its original level, indicating that low-temperature exposure did not compromise the operational stability of the device. As the temperature increased beyond 293 K, the G range expanded further, reaching saturation at 333 K. Upon further heating to 373 K, thermal activation likely enhanced ionic mobility, resulting in faster conductance saturation during potentiation and more rapid decay during depression. Nonetheless, stable and repeatable G modulation was maintained throughout the entire cycle. These results confirm that the 4gTT-2gT-based artificial synapse operates reliably across a wide temperature window, from cryogenic (233 K) to elevated temperatures (373 K). This level of thermal endurance is remarkable for organic electronic systems, featuring excellent low-temperature recovery and thermally enhanced dynamic range, comparable to that of state-of-the-art inorganic memristive devices.

3 | Conclusion

In summary, we employed a side-chain reorganization molecular design strategy, using a fused bithienothiophene in combination with bithiophene as the conjugated backbone, to develop a series of novel ion-electron mixed conductors with extended conjugation lengths, namely 3gTT-3gT, 4gTT-2gT, and 5gTT-1gT. The photophysical and electrochemical properties of these polymers were systematically investigated through spectroelectrochemistry and cyclic voltammetry measurements. Among them, 4gTT-2gT exhibited the highest OECT performance, achieving a high μC^* of 729 F V^{-1} cm^{-1} s^{-1}, a low threshold voltage of −0.04 V, a fast response times of 342 µs (τ_{on}) and 122 µs (τ_{off}), and excellent operational stability such that the device channel current still retained 94% of its initial value after 9 h of operation, ranking among the top-performing p-type OECT materials reported to date. Further structural investigations using EQCM-D, AFM, and GIWAXS revealed that side chain reorganization synergistically optimized ionic and electronic transport, enhancing doping efficiency, crystallinity, and mechanical stability. Without altering the conjugated backbone or total PEG content, the optimized polymer 4gTT-2gT formed a film structure that enabled fast ion transport and reversible morphology recovery, thereby supporting efficient mixed conduction. Finally, we demonstrated the excellent synaptic functionalities of 4gTT-2gT through a series of neuromorphic tests, including SADP, STDP, SNDP, PPF, and LTDP. Moreover, 4gTT-2gT-based ECRAM devices exhibited remarkable low temperature resilience and high temperature stability, maintaining stable LTDP operation across a wide temperature range. Our work highlights that side-chain reorganization represents a powerful strategy to engineer next-generation materials for low-power biosensors, wearable healthcare devices, and artificial synapses, significantly expanding the application boundaries of flexible electronics in biomedical and intelligent wearable technologies.

Acknowledgements

The authors thank King Abdullah University of Science and Technology (KAUST) Office of Sponsored Research (OSR) under Award Nos. OSR-2020-CRG8-4095 and ORFS-CRG12-2024-6443 for financial support. GIWAXS experiments were performed at NCD-SWEET beamline at ALBA Synchrotron (experiment ID AV-2024028192) with the collaboration of ALBA staff. The authors would also like to thank Ms. Yan Zhang for illustrating the TOC figure.

Conflicts of Interest

The authors declare no conflicts of interest.

Data Availability Statement

The data that support the findings of this study are available from the corresponding author upon reasonable request.

References

1. N. A. Kukhta, A. Marks, and C. K. Luscombe, "Molecular Design Strategies Toward Improvement of Charge Injection and Ionic Conduction in Organic Mixed Ionic–Electronic Conductors for Organic Electrochemical Transistors," *Chemical Reviews* 122 (2022): 4325–4355, https://doi.org/10.1021/acs.chemrev.1c00266.

2. D. T. Simon, E. O. Gabrielsson, K. Tybrandt, and M. Berggren, "Organic Bioelectronics: Bridging the Signaling Gap Between Biology and Technology," *Chemical Reviews* 116 (2016): 13009–13041, https://doi.org/10.1021/acs.chemrev.6b00146.

3. J. Rivnay, S. Inal, A. Salleo, R. M. Owens, M. Berggren, and G. G. Malliaras, "Organic Electrochemical Transistors," *Nature Reviews Materials* 3 (2018): 17086, https://doi.org/10.1038/natrevmats.2017.86.

4. Y. Wang, S. Wustoni, J. Surgailis, Y. Zhong, A. Koklu, and S. Inal, "Designing Organic Mixed Conductors for Electrochemical Transistor Applications," *Nature Reviews Materials* 9 (2024): 249–265, https://doi.org/10.1038/s41578-024-00652-7.

5. A. Nawaz, Q. Liu, W. L. Leong, K. E. Fairfull-Smith, and P. Sonar, "Organic Electrochemical Transistors for In Vivo Bioelectronics," *Advanced Materials* 33 (2021): 2101874, https://doi.org/10.1002/adma.202101874.

6. P. C. Harikesh, C. Y. Yang, H. Y. Wu, et al., "Ion-Tunable Antiambipolarity in Mixed Ion–Electron Conducting Polymers Enables Biorealistic Organic Electrochemical Neurons," *Nature Materials* 22 (2023): 242–248, https://doi.org/10.1038/s41563-022-01450-8.

7. X. Ji, B. D. Paulsen, G. K. K. Chik, et al., "Mimicking Associative Learning Using an Ion-Trapping Non-Volatile Synaptic Organic Electrochemical Transistor," *Nature Communications* 12 (2021): 2480, https://doi.org/10.1038/s41467-021-22680-5.

8. Y. Wang, W. Shan, H. Li, et al., "An Optoelectrochemical Synapse Based on a Single-Component n-type Mixed Conductor," *Nature Communications* 16 (2025): 1615, https://doi.org/10.1038/s41467-025-56814-w.

9. X. Ji, X. Lin, and J. Rivnay, "Organic Electrochemical Transistors as On-Site Signal Amplifiers for Electrochemical Aptamer-Based Sensing," *Nature Communications* 14 (2023): 1665, https://doi.org/10.1038/s41467-023-37402-2.

10. H. Sun, M. Vagin, S. Wang, et al., "Complementary Logic Circuits Based on High-Performance n-Type Organic Electrochemical Transistors," *Advanced Materials* 30 (2018): 1704916, https://doi.org/10.1002/adma.201704916.

11. S. Wang, X. Chen, C. Zhao, et al., "An Organic Electrochemical Transistor for Multi-Modal Sensing, Memory and Processing," *Nature Electronics* 6 (2023): 281–291, https://doi.org/10.1038/s41928-023-00950-y.

12. Y. Yao, W. Huang, J. Chen, et al., "Flexible and Stretchable Organic Electrochemical Transistors for Physiological Sensing Devices," *Advanced Materials* 35 (2023): 2209906, https://doi.org/10.1002/adma.202209906.

13. Y. Yao, R. M. Pankow, W. Huang, et al., "An Organic Electrochemical Neuron for a Neuromorphic Perception System," *Proceedings of the National Academy of Sciences* 122: 2414879122, https://doi.org/10.1073/pnas.2414879122.

14. P. Li, W. Sun, J. Li, et al., "N-type Semiconducting Hydrogel," *Science* 384 (2024): 557–563, https://doi.org/10.1126/science.adj4397.

15. A. Koklu, D. Ohayon, S. Wustoni, V. Druet, A. Saleh, and S. Inal, "Organic Bioelectronic Devices for Metabolite Sensing," *Chemical Reviews* 122 (2022): 4581–4635, https://doi.org/10.1021/acs.chemrev.1c00395.

16. A. Savva, R. Hallani, C. Cendra, et al., "Balancing Ionic and Electronic Conduction for High-Performance Organic Electrochemical Transistors," *Advanced Functional Materials* 30 (2020): 1907657, https://doi.org/10.1002/adfm.201907657.

17. L. Q. Flagg, C. G. Bischak, J. W. Onorato, R. B. Rashid, C. K. Luscombe, and D. S. Ginger, "Polymer Crystallinity Controls Water Uptake in Glycol Side-Chain Polymer Organic Electrochemical Transistors," *Journal of the American Chemical Society* 141 (2019): 4345–4354, https://doi.org/10.1021/jacs.8b12640.

18. B. Ding, I.-Y. Jo, M.-H. Yoon, and M. Heeney, "Designing Organic Mixed Ionic-Electronic Conductors With Low Environmental Footprint for Bioelectronics and Energy Storage," *Materials Science and Engineering: R: Reports* 164 (2025): 100974, https://doi.org/10.1016/j.mser.2025.100974.

19. Y. He, N. A. Kukhta, A. Marks, and C. K. Luscombe, "The Effect of Side Chain Engineering on Conjugated Polymers in Organic Electrochemical Transistors for Bioelectronic Applications," *Journal of Materials Chemistry C* 10 (2022): 2314–2332, https://doi.org/10.1039/D1TC05229B.

20. M. Moser, L. R. Savagian, A. Savva, et al., "Ethylene Glycol-Based Side Chain Length Engineering in Polythiophenes and its Impact on Organic Electrochemical Transistor Performance," *Chemistry of Materials* 32 (2020): 6618–6628, https://doi.org/10.1021/acs.chemmater.0c02041.

21. B. T. DiTullio, L. R. Savagian, O. Bardagot, et al., "Effects of Side-Chain Length and Functionality on Polar Poly(dioxythiophene)s for Saline-Based Organic Electrochemical Transistors," *Journal of the American Chemical Society* 145 (2023): 122, https://doi.org/10.1021/jacs.2c08850.

22. H. Liao, A. Savva, A. V. Marsh, et al., "High Performance Organic Mixed Ionic-Electronic Polymeric Conductor With Stability to Autoclave Sterilization," *Angewandte Chemie International Edition* 64 (2025): 202416288, https://doi.org/10.1002/anie.202416288.

23. O. Bardagot, B. T. DiTullio, A. L. Jones, J. Speregen, J. R. Reynolds, and N. Banerji, "Balancing Electroactive Backbone and Oligo(Ethylene Oxy) Side-Chain Content Improves Stability and Performance of Soluble PEDOT Copolymers in Organic Electrochemical Transistors," *Advanced Functional Materials* 35 (2024): 2412554, https://doi.org/10.1002/adfm.202412554.

24. Y. Wang, E. Zeglio, H. Liao, et al., "Hybrid Alkyl–Ethylene Glycol Side Chains Enhance Substrate Adhesion and Operational Stability in Accumulation Mode Organic Electrochemical Transistors," *Chemistry of Materials* 31 (2019): 9797–9806, https://doi.org/10.1021/acs.chemmater.9b03798.

25. H. Yu, A. Marks, S. M. Tuladhar, et al., "The Influence of Alkyl Spacers and Molecular Weight on the Charge Transport and Storage Properties of Oxy-Bithiophene-Based Conjugated Polymers," *Angewandte Chemie International Edition* 64 (2025): 202417897, https://doi.org/10.1002/anie.202417897.

26. I. P. Maria, B. D. Paulsen, A. Savva, et al., "The Effect of Alkyl Spacers on the Mixed Ionic-Electronic Conduction Properties of N-Type Polymers," *Advanced Functional Materials* 31 (2021): 2008718, https://doi.org/10.1002/adfm.202008718.

27. A. A. Szumska, I. P. Maria, L. Q. Flagg, et al., "Reversible Electrochemical Charging of n-Type Conjugated Polymer Electrodes in Aqueous Electrolytes," *Journal of the American Chemical Society* 143 (2021): 14795–14805, https://doi.org/10.1021/jacs.1c06713.

28. N. Siemons, D. Pearce, H. Yu, et al., "Controlling Swelling in Mixed Transport Polymers Through Alkyl Side-Chain Physical Cross-Linking," *Proceedings of the National Academy of Sciences* 120 (2023): 2306272120, https://doi.org/10.1073/pnas.2306272120.

29. A. Khot and B. M. Savoie, "How Side-Chain Hydrophilicity Modulates Morphology and Charge Transport in Mixed Conducting Polymers," *Journal of Polymer Science* 60 (2021): 610–620, https://doi.org/10.1002/pol.20210773.

30. A. Giovannitti, I. P. Maria, D. Hanifi, et al., "The Role of the Side Chain on the Performance of N-type Conjugated Polymers in Aqueous Electrolytes," *Chemistry of Materials* 30 (2018): 2945–2953, https://doi.org/10.1021/acs.chemmater.8b00321.

31. M. Moser, T. C. Hidalgo, J. Surgailis, et al., "Side Chain Redistribution as a Strategy to Boost Organic Electrochemical Transistor Performance and Stability," *Advanced Materials* 32 (2020): 2002748, https://doi.org/10.1002/adma.202002748.

32. B. Ding, G. Kim, Y. Kim, et al., "Influence of Backbone Curvature on the Organic Electrochemical Transistor Performance of Glycolated Donor–Acceptor Conjugated Polymers," *Angewandte Chemie International Edition* 60 (2021): 19679–19684, https://doi.org/10.1002/anie.202106084.

33. H. Jia, Z. Huang, P. Li, et al., "Engineering Donor–Acceptor Conjugated Polymers for High-Performance and Fast-Response Organic Electrochemical Transistors," *Journal of Materials Chemistry C* 9 (2021): 4927–4934, https://doi.org/10.1039/D1TC00440A.

34. M. Moser, A. Savva, K. Thorley, et al., "Polaron Delocalization in Donor–Acceptor Polymers and its Impact on Organic Electrochemical Transistor Performance," *Angewandte Chemie International Edition* 60 (2021): 7777–7785, https://doi.org/10.1002/anie.202014078.

35. Y. Wang, A. Hamidi-Sakr, J. Surgailis, et al., "The Effect of the Donor Moiety of DPP Based Polymers on the Performance of Organic Electrochemical Transistors," *Journal of Materials Chemistry C* 9 (2021): 13338–13346, https://doi.org/10.1039/D1TC02994K.

36. I. Y. Jo, D. Jeong, Y. Moon, et al., "High-Performance Organic Electrochemical Transistors Achieved by Optimizing Structural and Energetic Ordering of Diketopyrrolopyrrole-Based Polymers," *Advanced Materials* 36 (2024): 2307402, https://doi.org/10.1002/adma.202307402.

37. A. Giovannitti, D. T. Sbircea, S. Inal, et al., "Controlling the Mode of Operation Of Organic Transistors Through Side-Chain Engineering," *Proceedings of the National Academy of Sciences* 113 (2016): 12017–12022, https://doi.org/10.1073/pnas.1608780113.

38. C. B. Nielsen, A. Giovannitti, D. T. Sbircea, et al., "Molecular Design of Semiconducting Polymers for High-Performance Organic Electrochemical Transistors," *Journal of the American Chemical Society* 138 (2016): 10252–10259, https://doi.org/10.1021/jacs.6b05280.

39. I. McCulloch, M. Heeney, M. L. Chabinyc, et al., "Semiconducting Thienothiophene Copolymers: Design, Synthesis, Morphology, and Performance in Thin-Film Organic Transistors," *Advanced Materials* 21 (2009): 1091–1109, https://doi.org/10.1002/adma.200801650.

40. P. Brocorens, A. Van Vooren, M. L. Chabinyc, et al., "Solid-State Supramolecular Organization of Polythiophene Chains Containing Thienothiophene Units," *Advanced Materials* 21 (2009): 1193–1198, https://doi.org/10.1002/adma.200801668.

41. J. Kimpel, Y. Kim, J. Asatryan, J. Martin, R. Kroon, and C. Muller, "High-mobility Organic Mixed Conductors With a Low Synthetic Complexity Index via Direct Arylation Polymerization," *Chemical Science* 15 (2024): 7679–7688, https://doi.org/10.1039/D4SC01430H.

42. B. Ding, V. Le, H. Yu, et al., "Development of Synthetically Accessible Glycolated Polythiophenes for High-Performance Organic Electrochemical Transistors," *Advanced Electronic Materials* 10 (2024): 2300580, https://doi.org/10.1002/aelm.202300580.

43. B. Ding, I. Y. Jo, H. Yu, et al., "Enhanced Organic Electrochemical Transistor Performance of Donor–Acceptor Conjugated Polymers Modified With Hybrid Glycol/Ionic Side Chains by Postpolymerization Modification," *Chemistry of Materials* 35 (2023): 3290–3299, https://doi.org/10.1021/acs.chemmater.3c00327.

44. R. Hildner, A. Köhler, P. Müller-Buschbaum, F. Panzer, and M. Thelakkat, "π-Conjugated Donor Polymers: Structure Formation and Morphology in Solution, Bulk and Photovoltaic Blends," *Advanced Energy Materials* 7 (2017): 1700314, https://doi.org/10.1002/aenm.201700314.

45. C. Enengl, S. Enengl, S. Pluczyk, et al., "Doping-Induced Absorption Bands in P3HT: Polarons and Bipolarons," *Chemphyschem* 17 (2016): 3836–3844, https://doi.org/10.1002/cphc.201600961.

46. M. S. A. Abdou, F. P. Orfino, Y. Son, and S. Holdcroft, "Interaction of Oxygen With Conjugated Polymers: Charge Transfer Complex Formation With Poly(3-alkylthiophenes)," *Journal of the American Chemical Society* 119 (1997): 4518–4524, https://doi.org/10.1021/ja964229j.

47. I. Zozoulenko, A. Singh, S. K. Singh, V. Gueskine, X. Crispin, and M. Berggren, "Polarons, Bipolarons, and Absorption Spectroscopy of PEDOT," *ACS Applied Polymer Materials* 1 (2018): 83–94, https://doi.org/10.1021/acsapm.8b00061.

48. S. Ghosh, V. Gueskine, M. Berggren, and I. V. Zozoulenko, "Electronic Structures and Optical Absorption of N-Type Conducting Polymers at Different Doping Levels," *The Journal of Physical Chemistry C* 123 (2019): 15467–15476, https://doi.org/10.1021/acs.jpcc.9b04634.

49. P. Cavassin, I. Holzer, D. Tsokkou, O. Bardagot, J. Rehault, and N. Banerji, "Electrochemical Doping in Ordered and Disordered Domains of Organic Mixed Ionic–Electronic Conductors," *Advanced Materials* 35 (2023): 2300308, https://doi.org/10.1002/adma.202300308.

50. T. Schoetz, L. W. Gordon, S. Ivanov, A. Bund, D. Mandler, and R. J. Messinger, "Disentangling faradaic, pseudocapacitive, and capacitive charge storage: A tutorial for the characterization of batteries, supercapacitors, and hybrid systems," *Electrochimica Acta* 412 (2022): 140072, https://doi.org/10.1016/j.electacta.2022.140072.

51. M. Xie, H. Liu, M. Wu, et al., "Cycling Stability of Organic Electrochemical Transistors," *Organic Electronics* 117 (2023): 106777, https://doi.org/10.1016/j.orgel.2023.106777.

52. V. Venkatraman, J. T. Friedlein, A. Giovannitti, et al., "Subthreshold Operation of Organic Electrochemical Transistors for Biosignal Amplification," *Advanced Science* 5 (2018): 1800453, https://doi.org/10.1002/advs.201800453.

53. P. Li and T. Lei, "Toward Ideal Biointerfacing Electronics Using Organic Electrochemical Transistors," *Accounts of Materials Research* 6 (2025): 853–864.

54. D. Ohayon, V. Druet, and S. Inal, "A Guide for the Characterization of Organic Electrochemical Transistors and Channel Materials," *Chemical Society Reviews* 52 (2023): 1001–1023, https://doi.org/10.1039/D2CS00920J.

55. V. N. Le, K. N. Baustert, M. R. Brown, et al., "Improved Organic Electrochemical Transistor Stability Using Solvent Degassing and Chemical Doping," *Nature Electronics* 8 (2025): 116–126.

56. S. T. Keene, L. W. Gatecliff, S. L. Bidinger, M. Moser, I. McCulloch, and G. G. Malliaras, "Stable Operating Windows for Polythiophene Organic Electrochemical Transistors," *MRS Communications* 14 (2023): 158–166, https://doi.org/10.1557/s43579-023-00511-6.

57. E. A. Schafer, R. Wu, D. Meli, et al., "Sources and Mechanism of Degradation in p-Type Thiophene-Based Organic Electrochemical Transistors," *ACS Applied Electronic Materials* 4 (2022): 1391–1404, https://doi.org/10.1021/acsaelm.1c01171.

58. P. Gkoupidenis, Y. Zhang, H. Kleemann, et al., "Organic Mixed Conductors for Bioinspired Electronics," *Nature Reviews Materials* 9 (2023): 134–149, https://doi.org/10.1038/s41578-023-00622-5.

59. A. Melianas, T. J. Quill, G. LeCroy, et al., "Temperature-Resilient Solid-State Organic Artificial Synapses for Neuromorphic Computing," *Science Advances* 6 (2020): abb2958, https://doi.org/10.1126/sciadv.abb2958.

60. R. Liu, X. Zhu, J. Duan, et al., "Versatile Neuromorphic Modulation and Biosensing based on N-type Small-molecule Organic Mixed Ionic-Electronic Conductors," *Angewandte Chemie International Edition* 63 (2024): 202315537, https://doi.org/10.1002/anie.202315537.

61. R. B. Rashid, X. Ji, and J. Rivnay, "Organic Electrochemical Transistors in Bioelectronic Circuits," *Biosensors and Bioelectronics* 190 (2021): 113461, https://doi.org/10.1016/j.bios.2021.113461.

62. Y. Zhao, C. Su, G. Shen, et al., "Donor Engineering Tuning the Analog Switching Range and Operational Stability of Organic Synaptic Transistors for Neuromorphic Systems," *Advanced Functional Materials* 32 (2022): 2205744, https://doi.org/10.1002/adfm.202205744.

63. Y. Zhao, S. Haseena, M. K. Ravva, et al., "Side Chain Engineering Enhances the High-Temperature Resilience and Ambient Stability of Organic Synaptic Transistors for Neuromorphic Applications," *Nano Energy* 104 (2022): 107985, https://doi.org/10.1016/j.nanoen.2022.107985.

64. H. Roh, S. Yue, H. Hu, K. Chen, H. J. Kulik, and A. Gumyusenge, "Unraveling Polymer–Ion Interactions in Electrochromic Polymers for their Implementation in Organic Electrochemical Synaptic Devices," *Advanced Functional Materials* 33 (2023): 2304893, https://doi.org/10.1002/adfm.202304893.

Supporting Information

Additional supporting information can be found online in the Supporting Information section.

Supporting file: adma71838-sup-0001-SuppMat.docx.